



Article

Ultra-Fast Construction of Novel S-Scheme $\text{CuBi}_2\text{O}_4/\text{CuO}$ Heterojunction for Selectively Photocatalytic CO_2 Conversion to CO

Weina Shi ¹, Xiu Qiao ², Jichao Wang ^{2,*} , Miao Zhao ¹, Hongling Ge ², Jingjing Ma ², Shanqin Liu ² and Wanqing Zhang ^{2,*}

¹ School of Chemistry and Materials Engineering, Xinxiang University, Xinxiang 453000, China

² College of Chemistry and Chemical Engineering, Henan Institute of Science and Technology, Xinxiang 453000, China

* Correspondence: wangjichao@hist.edu.cn (J.W.); zhangwqzzu@163.com (W.Z.);
Tel.: +86-0373-304-0418 (J.W. & W.Z.)

Abstract: Herein, step-scheme (S-scheme) $\text{CuBi}_2\text{O}_4/\text{CuO}$ (CBO/ CuO) composite films were successfully synthesized on glass substrates by the ultra-fast spraying-calcination method. The photocatalytic activities of the obtained materials for CO_2 reduction in the presence of H_2O vapor were evaluated under visible light irradiation ($\lambda > 400$ nm). Benefiting from the construction of S-scheme heterojunction, the CO, CH_4 and O_2 yields of the optimal CBO/ CuO composite reached 1599.1, 5.1 and 682.2 $\mu\text{mol}/\text{m}^2$ after irradiation for 9 h, and the selectivity of the CO product was notably enhanced from below 18.5% to above 98.5% compared with those of the bare samples. In the sixth cycling experiment, the yields of main products decreased by less than 15%, and a high CO selectivity was still kept. The enhanced photocatalytic performance of CO_2 reduction was attributed to the efficient separation of photogenerated charge carriers. Based on the photocatalytic activity, band structure and in situ-XPS results, the S-scheme charge transfer mechanism was conformed. The study provides an insight into the design of S-scheme photocatalysts for selective CO_2 conversion.

Keywords: CO_2 reduction; photocatalyst; selectivity; $\text{CuBi}_2\text{O}_4/\text{Cu}_2\text{O}$; S-scheme



Citation: Shi, W.; Qiao, X.; Wang, J.; Zhao, M.; Ge, H.; Ma, J.; Liu, S.; Zhang, W. Ultra-Fast Construction of Novel S-Scheme $\text{CuBi}_2\text{O}_4/\text{CuO}$ Heterojunction for Selectively Photocatalytic CO_2 Conversion to CO. *Nanomaterials* **2022**, *12*, 3247. <https://doi.org/10.3390/nano12183247>

Academic Editor: Antonino Gulino

Received: 17 August 2022

Accepted: 15 September 2022

Published: 19 September 2022

Publisher's Note: MDPI stays neutral with regard to jurisdictional claims in published maps and institutional affiliations.



Copyright: © 2022 by the authors. Licensee MDPI, Basel, Switzerland. This article is an open access article distributed under the terms and conditions of the Creative Commons Attribution (CC BY) license (<https://creativecommons.org/licenses/by/4.0/>).

1. Introduction

Photocatalytic reduction of CO_2 into valuable chemicals utilizing H_2O and solar energy is considered to be a promising strategy for addressing energy shortage and greenhouse effect issues. On the basis of that, substantial efforts have been devoted to developing highly efficient photocatalysts, and copper-containing oxide photocatalysts are particularly relevant for CO_2 reduction, including CuO , Cu_2O , CuBi_2O_4 , CuFe_2O_4 , CuFeO_2 , CuV_3O_4 , $\text{Cu}_3\text{Nb}_2\text{O}_8$, CuGaO_2 , and so on [1]. Among the above encouraging photocatalysts, CuBi_2O_4 is an attractive candidate in terms of its suitable band gap (1.5–2.0 eV) and relatively negative conduction band edge position [1]. However, the major hurdle for CuBi_2O_4 lies in its valance band potential, which is more positive than the $\text{H}_2\text{O}/\text{O}_2$ potential, indicating its main application in the field of photoelectrocatalysis rather than photocatalytic CO_2 reduction with H_2O [2]. Hence, it is necessary to devise CuBi_2O_4 -based composite catalysts with a high conversion efficiency and controllable selectivity for photocatalytic CO_2 reduction.

The formation of a heterojunction structure by coupling CuBi_2O_4 with other semiconductors is a feasible strategy for photocatalyst modification [3]. Particularly, the construction of a S-scheme heterojunction can preserve strong redox abilities and achieve an efficient separation of charge carriers in comparison with the traditional type II heterojunction, enhancing photocatalytic activity and product selectivity for CO_2 reduction [4–7]. For instance, CuBi_2O_4 -based S-scheme systems such as $\text{BiOCl}/\text{CuBi}_2\text{O}_4$ [8], $\text{CuBi}_2\text{O}_4/\text{BiOBr}$ [9], $\text{CuBi}_2\text{O}_4/\text{CoV}_2\text{O}_6$ [10] and $\text{CuBi}_2\text{O}_4/\text{Bi}_4\text{O}_5\text{I}_2$ [11] have been reported to boost photocatalytic performances. Our previous work demonstrated that the synthesized S-scheme

CuBi₂O₄/Bi₂O₃ heterojunction exhibited enhanced CO and CH₄ yields for CO₂ photoreduction in water vapor [2]. We further reported the construction of a S-scheme WO₃/CuBi₂O₄ photocatalyst for a visible-light-driven CO₂ reduction with a good photocatalytic activity and stability [12]. As a typical transition metal oxide, CuO has been demonstrated to be feasible for heterojunction construction due to its narrow band gap (1.4–1.8 eV) and suitable band edge position [13], and heterostructures including CuO/TiO₂ [14], CuO/ZnO [15], WO₃/CuO [16,17], CuO/BiOCl [18], CuO/g-C₃N₄ [19] and Nb₂O₅/CuO [20] have been adopted for efficient photocatalytic CO₂ photoreduction. For instance, Nogueira et al. reported that compositing Nb₂O₅ with increased amounts of CuO led to a higher selectivity for CH₄ production [20]. Therefore, in view of the above analysis, it is of significance to rationally construct the heterojunction catalyst by combining CuO and CuBi₂O₄. Recently, CuO/CuBi₂O₄ heterojunction has been studied for photoelectrocatalysis [21–23], photodegradation [24] and electrochemical detection [25]. However, to date, few studies have been conducted to construct CuO/CuBi₂O₄ heterojunction for photocatalytic CO₂ reduction with H₂O vapor, a system in which the limited solubility of CO₂ in the solvent or weak CO₂ adsorption ability will be overcome.

In this work, a series of CuO/CuBi₂O₄ heterojunction composites with different molar ratios were synthesized onto glass substrates by ultra-fast spray pyrolysis followed by annealing treatment. The heterojunction catalysts were investigated for photocatalytic CO₂ reduction with H₂O vapor. The CuO/CuBi₂O₄ composites exhibited a superior photocatalytic performance than those of the single CuO and CuBi₂O₄, and the enhanced ratio of CuBi₂O₄ in the heterojunction benefited the improved product selectivity of CO₂ photoreduction into CO. Based on the experimental and theoretical results, the S-scheme charge transfer mechanism was proposed and discussed in detail.

2. Materials and Methods

2.1. Materials Synthesis

In the typical synthesis of the CuBi₂O₄/CuO sample, 2.6180 g of Cu(NO₃)₂·3H₂O was firstly dissolved into 20 mL of ethanol, and 2.4250 g of Bi(NO₃)₃·5H₂O was dissolved into 4 mL of nitric acid with the subsequent addition of deionized water (16 mL). The precursor solution for spraying was obtained by mixing the above two solutions. The glass substrate (2.1 cm × 2.3 cm) was pre-cleaned in H₂O₂ solution and irradiated by UV light for 30 min, followed by immobilization onto the heating stage under 280 °C, and then the precursor solution was sprayed on the above substrate with 0.3 MPa N₂ pressure. The obtained precursor film was heated at 480 °C for 2 h in air. Finally, the CuBi₂O₄/CuO composite was obtained and named as 30CBO/CuO (30 represented the ideal molar ratio between CuBi₂O₄ and CuO). In addition, the other CBO/CuO composites with different ratios of two components were similarly synthesized by spraying the precursor solutions with variations in the contents of Cu(NO₃)₂·3H₂O and Bi(NO₃)₃·5H₂O. For comparison, the bare CuO and CuBi₂O₄ samples were synthesized based on the stoichiometric mole ratios of Cu and Bi in the precursor solutions. Simultaneously, the 30CBO/CuO-m sample was obtained by mechanically mixing the bare CuO and CuBi₂O₄ nanoparticles with a molar ratio of 0.3.

2.2. Characterization

The crystal structures of the as-prepared samples were studied by X-ray diffraction (XRD, BRUKER D8 Advance). The morphology and structure were inspected with scanning electron microscopy (SEM, FEI Quanta 250 FEG) and transmission electron microscopy (TEM, FEI Talos F200X). The chemical states were investigated by X-ray photoelectron spectroscopy (XPS, Escalab XI+, Thermofisher Scientific, Santa Clara, CA, USA). The optical properties of the obtained photocatalysts were obtained on a UV-vis spectrophotometer (Cary 5000, Agilent, Santa Clara, CA, USA). The photocurrent responses and electrochemical impedance spectroscopy were measured by an electrochemical workstation (CHI660E, CH Instruments Ins., Shanghai, China).

2.3. Photocatalytic Performance for CO₂ Reduction

The photocatalytic performance for CO₂ reduction with H₂O vapor was measured in the reactor with a top quartz window. A 300 W Xenon arc lamp (CEL-HXF300, Beijing China Education Au-light Co., Ltd., Beijing, China) with an UV cutoff filter ($\lambda > 400$ nm) was utilized as the light source. The glass substrate with the composite catalyst was placed inside the stainless steel cylindrical vessel reactor (CEL-GPRT100, Beijing China Education Au-light Co., Ltd., China). Prior to light irradiation, the reaction setup was purged with high purity CO₂ gas (99.999%) several times. The compressed high-purity CO₂ gas was passed through a water bubbler to generate a mixture of CO₂ and H₂O vapor. After illumination, the gaseous products were quantitatively identified for off-line analysis using the gas chromatograph (GC-7920, Beijing China Education Au-light Co., Ltd., China) equipped with a flame ionized detector (FID) and GC-MS (Agilent 7890A-5975C) with a thermal conductivity detector (TCD), and the equipped columns were TDX-01 and Porapak-Q, respectively. Blank tests were conducted in the absence of photocatalysts and in the dark with catalysts. No products were detected, indicating that the presence of both visible-light irradiation and the photocatalyst were indispensable for the photocatalytic reduction of CO₂ with H₂O vapor. The product selectivity (*S*) for CO₂ reduction was calculated with the following equations (Equations (1) and (2)):

$$S_{\text{CO}} (\%) = 2 \times N_{\text{CO}} / (2 \times N_{\text{CO}} + 8 \times N_{\text{CH}_4}) \times 100 \quad (1)$$

$$S_{\text{CH}_4} (\%) = 2 \times N_{\text{CH}_4} / (2 \times N_{\text{CO}} + 8 \times N_{\text{CH}_4}) \times 100 \quad (2)$$

N_{CO} and N_{CH_4} represented the yield of detected CO and CH₄ molecules, respectively. To evaluate the stability, the 30CBO/CuO model sample was refreshed by washing with deionized water, and its photocatalytic performance was reevaluated in the aforementioned conditions.

3. Results and Discussion

3.1. Structure, Composition and Morphology

Figure 1a shows the XRD patterns of the as-prepared samples. Several diffraction peaks were distinctly discovered at 35.5, 38.7, 48.7 and 61.5°, which corresponded to the (−1 1 1), (1 1 1), (−2 0 2) and (−1 1 3) crystal faces of monoclinic CuO (PDF card No. 00-041-0254). Meanwhile, the diffraction peaks of the CuBi₂O₄ sample matched perfectly with those of tetragonal CuBi₂O₄ (PDF card No. 01-072-0493). Simultaneously, the peak intensity of CuBi₂O₄ in the CBO/CuO composites, which was labeled by a green dotted line in Figure 1a, gradually increased with increasing molar ratios of CuBi₂O₄. Except for the diffraction peaks of CuBi₂O₄ and CuO, no other peaks were detected in the composites, which indicated that the CBO/CuO composite was composed of monoclinic CuO and tetragonal CuBi₂O₄. XPS measurements were further conducted to explore the composition of the obtained samples. As shown in Figure S1a, the Cu, Bi, O and C elements existed in the CBO and composite samples, while Cu, O and C elements appeared in the CuO sample. The C element was attributed to the adsorbed CO₂ molecules on the surface. In the high-resolution Cu 2p XPS spectra (Figure 1b) of the CBO/CuO composite, two peaks were observed at binding energies of 933.84 eV for Cu(II) 2p 3/2 and 953.83 eV for Cu(II) 2p 1/2 [26,27]. Furthermore, the conspicuous peaks at binding energies of 158.84 and 164.15 eV in the Bi 4f spectra (Figure 1c) were ascribed to the Bi(III) state of CuBi₂O₄ [28,29]. It was notable that a slight shift of the characteristic peak position appeared for the 30CBO/CuO composite when compared with those of the bare CuBi₂O₄ and CuO samples, which was caused by the formation of a heterojunction between the two components. The O 1s spectrum of CBO/CuO is shown in Figure S1b, and the two peaks at 530.1 and 529.6 eV were ascribed to lattice oxygen of CuO and CuBi₂O₄ materials. Other peaks at 531.2 and 532.5 eV were assigned to intrinsic oxygen defects and surface adsorbed oxygen, respectively [20,24,30].

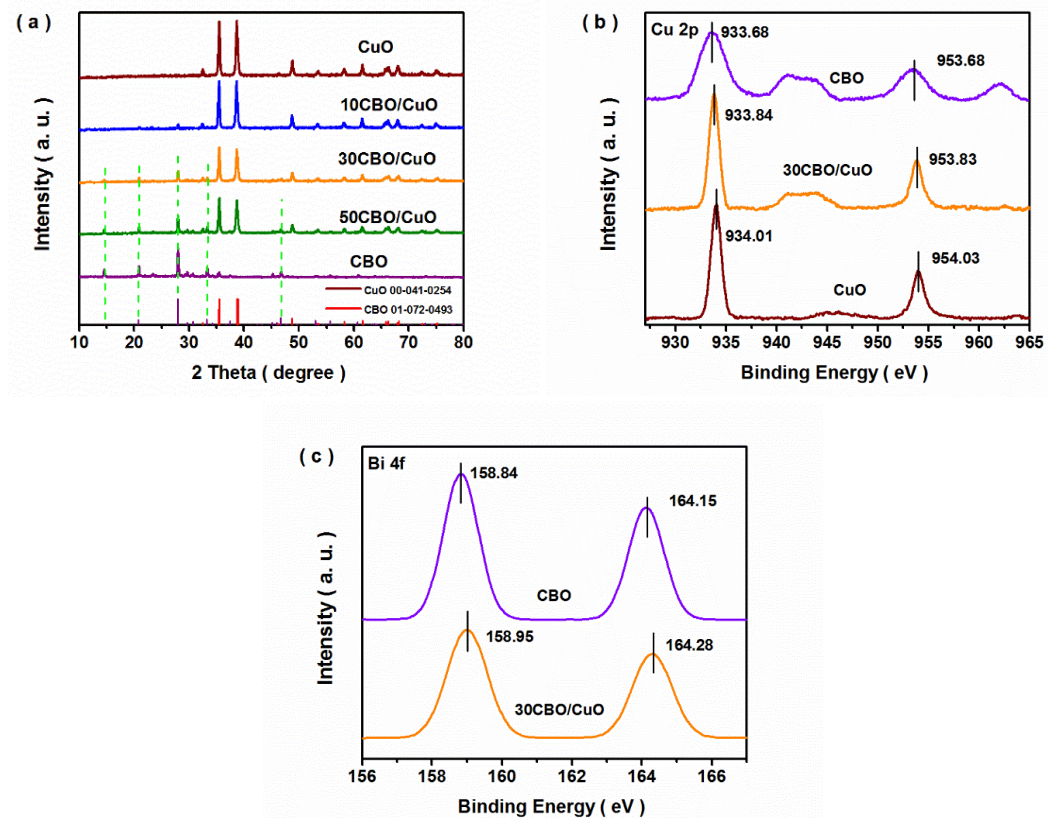


Figure 1. XRD patterns (a) and XPS spectra ((b) Cu 2p and (c) Bi 4f) of the as-prepared samples.

The morphologies of the as-prepared CuBi_2O_4 , CuO and 30CBO/CuO samples were visualized via SEM and TEM characterizations. The SEM images in Figure 2a–c demonstrated that all the samples exhibited the typical particle morphology. Concurrently, a lot of voids were formed due to piles of particles, leading to large exposed surfaces. TEM measurements were further conducted to determine the accurate sizes of CuO and CuBi_2O_4 particles, which were obtained from the substrates by ultrasound methods. As shown in Figure S2, the size distribution of CuO and CuBi_2O_4 nanoparticles basically obeyed the logical normal distribution, and their average particle sizes were about 47.7 and 26.6 nm, respectively. The TEM image of 30CBO/CuO in Figure 2d shows two groups of particles with different sizes. In the HRTEM image (Figure 2e), the distinct lattice spacings of 0.275 and 0.268 nm were indexed to the (1 0 2) and (3 1 0) crystal faces of tetragonal CuBi_2O_4 , and lattice spacings of 0.138, 0.137 and 0.120 nm were also discovered, which were assigned to the (1 1 3), (2 2 0) and (2 0 4) planes of monoclinic CuO. Additionally, the EDX mapping images in Figure 2f showed that the Cu, Bi and O elements were uniformly distributed. The above SEM and TEM observations, combined with the XRD and XPS results, revealed that both monoclinic-phase CuO and tetragonal-phase CuBi_2O_4 were present and fused at the interface.

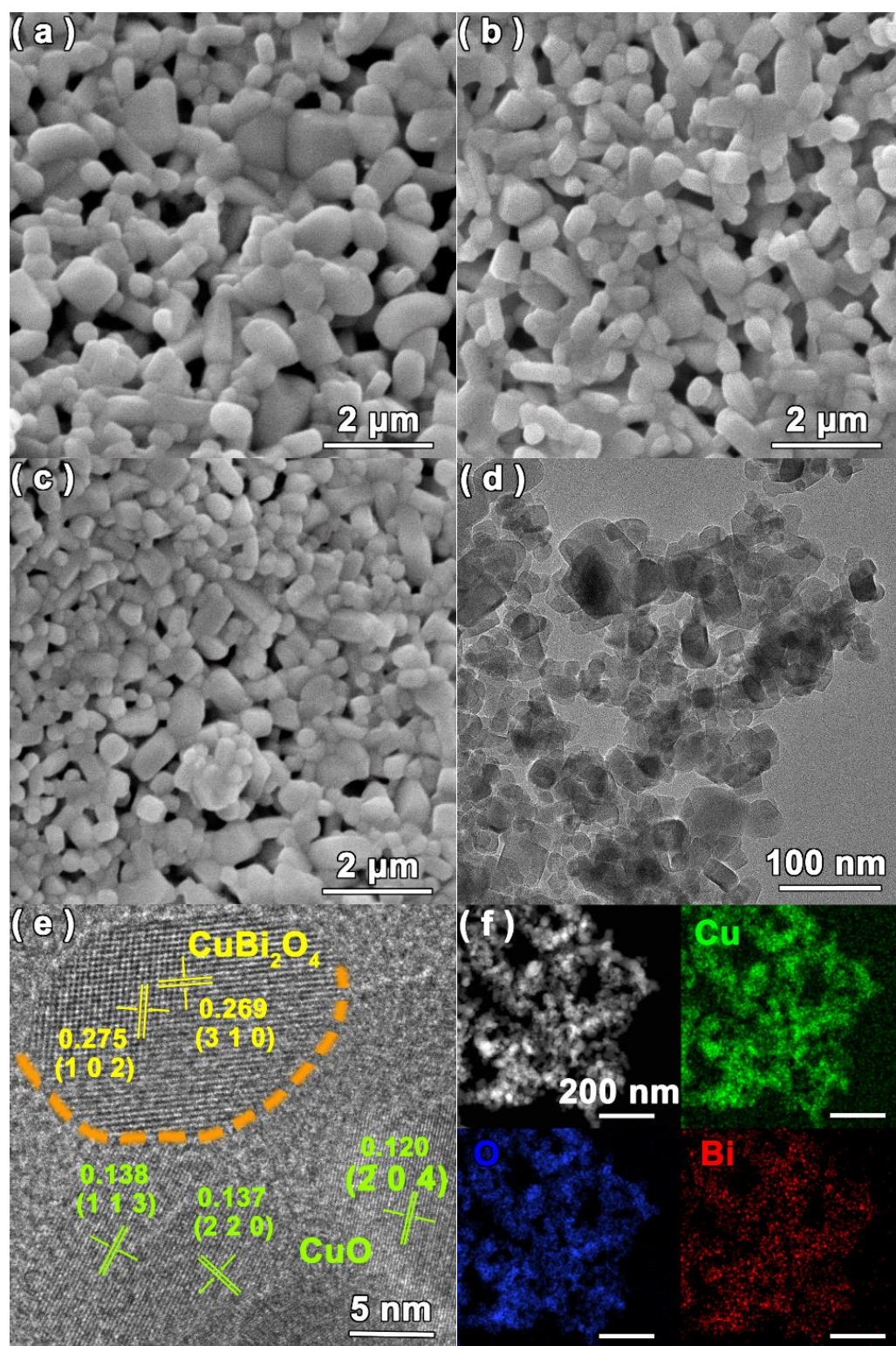


Figure 2. SEM images of (a) CuBi_2O_4 , (b) CuO and (c) 30CBO/ CuO samples; (d) TEM image, (e) HRTEM image and (f) EDX mapping images of the 30CBO/ CuO sample.

To further explore the band structure of heterojunction, the DRS and VB-XPS results were gained and are shown in Figure 3. As shown in Figure 3a, the bare and composite samples showed a strong absorption in the visible light region, indicating the feasibility of a visible-light utilization for photocatalytic CO_2 reduction. The band gaps (E_g) of the samples were estimated by the plots of $(\alpha h\nu)^n$ versus photo energy ($h\nu$), considering that CuBi_2O_4

and CuO exhibited band-to-band excitations involving direct and indirect transitions, respectively [20,31]. The E_g values of CuBi_2O_4 and CuO were respectively calculated to be 1.87 and 1.60 eV. According to the conventional method, the valence band (VB) positions of the CuBi_2O_4 and CuO samples (Figure 3b) were determined to be about 0.92 and 1.34 eV, respectively. Hence, their conduction band (CB) positions were calculated to be -0.95 and -0.26 eV, respectively. With the formation of the heterojunction, the alignment of the Fermi levels was assumed at the interfacial phases of the CBO/CuO composite. Accompanied by the movement of the Fermi levels, the CB and VB edge positions for both CuBi_2O_4 and CuO shifted. In this case, the band offsets of the CBO/CuO heterojunction can be calculated using the XPS core-level alignment method, according to the following equation [24,32]:

$$\Delta E_{\text{VB}} = (E_{\text{Bi}4f7/2,\text{CBO}} - E_{\text{VB,CBO}}) - (E_{\text{Cu}2p3/2,\text{CuO}} - E_{\text{VB,CuO}}) - (E_{\text{Bi}4f7/2,\text{CBO/CuO}} - E_{\text{Cu}2p3/2,\text{CBO/CuO}}) \quad (3)$$

$$\Delta E_{\text{CB}} = \Delta E_{\text{VB}} - E_{\text{gap,CBO}} + E_{\text{gap,CuO}} \quad (4)$$

where $E_{x,y}$ was denoted as the binding energy of the core level “x” or VB for the sample “y”, and $E_{\text{gap},y}$ referred to the values calculated from DRS. According to the above method and relevant data (Table S1), the ΔE_{VB} and ΔE_{CB} for the CBO/CuO composite were calculated to be about 0.23 and 0.15 eV. The corresponding band structure diagrams (Figure 3c,d) were schemed, and a staggered band alignment heterostructure was constructed.

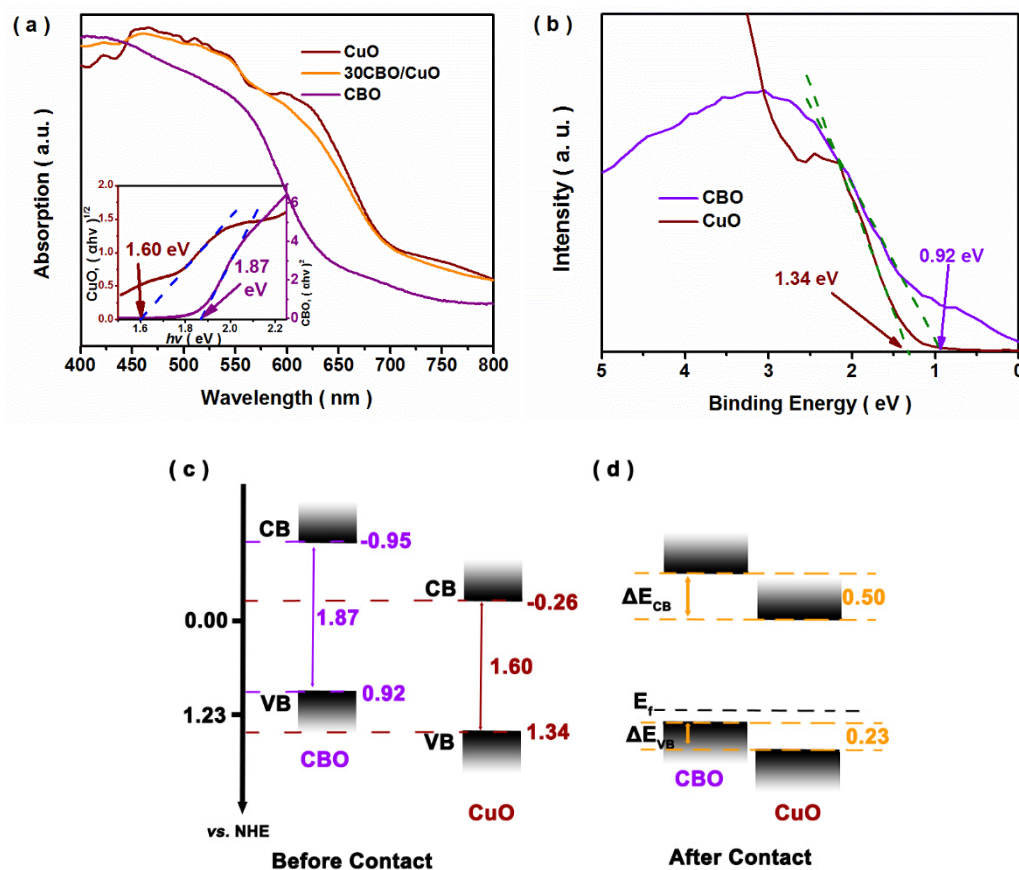


Figure 3. (a) DRS and (b) VB-XPS spectra of the as-prepared samples; and (c,d) schematic diagrams of the band structure for CBO/CuO heterojunction.

3.2. Photocatalytic Performance of CO_2 Reduction

The photocatalytic performances for CO_2 reduction were investigated under the mixed atmosphere of CO_2 and H_2O vapor. Figure 4a shows the production yields after 3 h of visible-light irradiation (>400 nm). The photocatalytic products for the bare CuO catalyst included CO, CH_4 and O_2 , while there were no detectable products for bare CuBi_2O_4 . The

CO, CH₄ and O₂ yields of 30CBO/CuO were the highest among the CBO/CuO composites with different ratios. Simultaneously, the CO selectivity was obviously enhanced with the increase of the CuBi₂O₄ content in the composite, reaching about 98% for the 30CBO/CuO catalyst. Compared with the photocatalytic activity of 30CBO/CuO-m (Figure S3), the enhanced yields were caused by the formation of a heterojunction in the 30CBO/CuO composite. CO, CH₄ and O₂ yields respectively reached 561.4, 2.1 and 232.2 $\mu\text{mol}/\text{m}^2$ after 3 h of visible-light illumination. The yields of the main products rapidly and regularly increased (Figure 4b) when prolonging the illumination time. After 9 h of visible-light illumination, the rate of CO and O₂ yields were still maintained at 177.7 and 75.8 $\mu\text{mol}/\text{m}^2/\text{h}$, respectively, and the CO selectivity was kept above 98.5%.

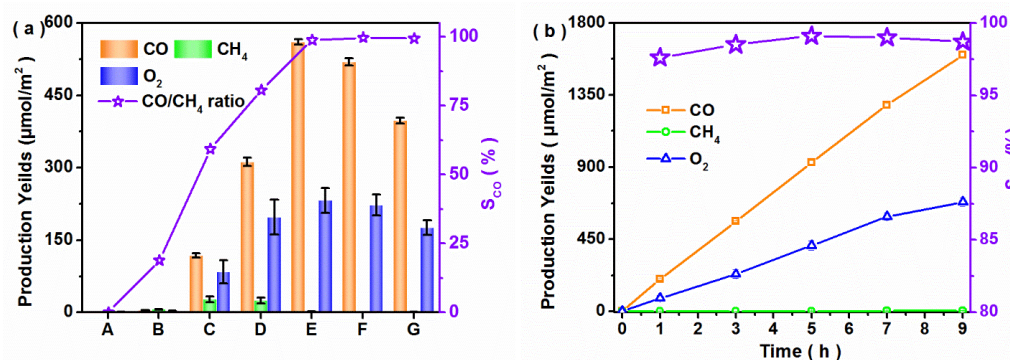


Figure 4. Photocatalytic activity for different samples under visible-light illumination ((a) A. CBO, B. CuO, C. 10CBO/CuO, D. 20CBO/CuO, E. 30CBO/CuO, F. 40 CBO/CuO, G. 50CBO/CuO. (b) 30CBO/CuO as catalyst).

The catalytic stability of the photocatalyst was never ignored in the practical application of CO₂ conversion. Figure 5a shows the cycling experiments of photocatalytic CO₂ reduction for the optimal 30CBO/CuO sample. In the sixth cycling experiment, all the product yields were reduced by under 15%, and the CO selectivity still reached over 98.5%. The XRD and XPS results of the used sample after the sixth cycling experiment are shown in Figure 5b–d. In the XRD patterns (Figure 5b), no other new diffraction peaks of the used 30CBO/CuO sample were observed when compared with those of the fresh sample. Similarly, there was no obvious difference between the fresh and used samples in the XPS spectra (Figure 5c,d). It was indicated that the 30CBO/CuO composite exhibited an excellent photocatalytic stability for CO₂ reduction with H₂O vapor.

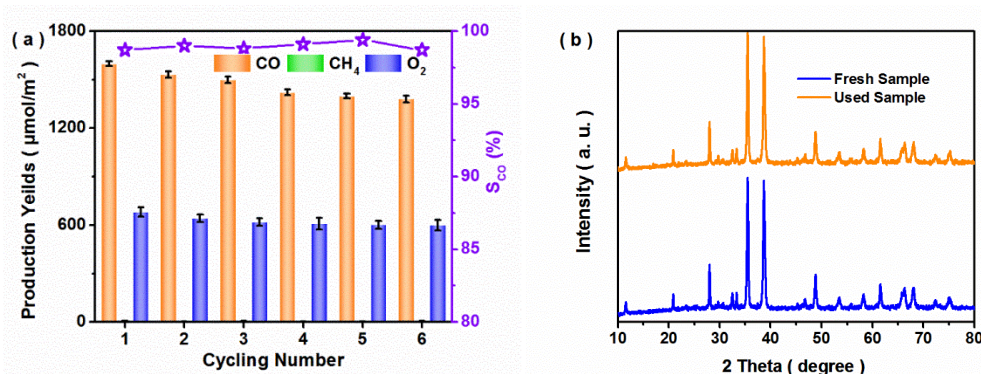


Figure 5. Cont.

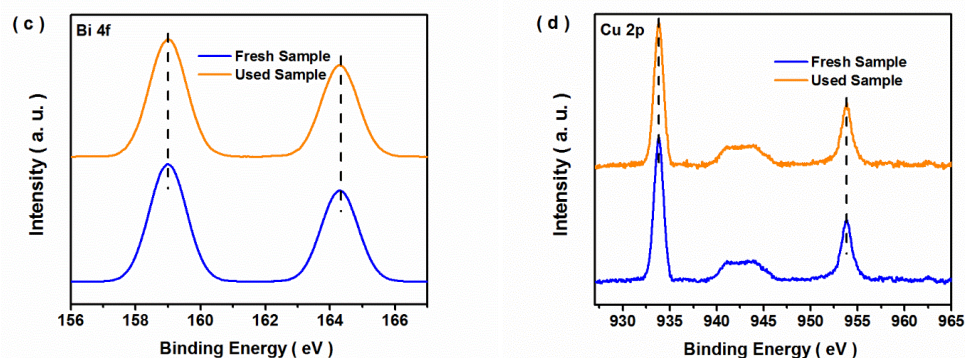


Figure 5. Photocatalytic activity (a) of 30CBO/CuO in the cycling experiment; (b) XRD pattern, (c) Bi 4f and (d) Cu 2p XPS spectra of the fresh and used 30CBO/CuO samples after the sixth cycling experiment.

Transient photocurrent responses were recorded for several on-off irradiation cycles to provide more convincing evidence for the separation of photoinduced carriers. As shown in Figure 6a, the photocurrent responses of all the samples reproducibly increased under each irradiation and quickly recovered in the dark. Furthermore, the transient photocurrent of 30CBO/CuO was higher than those of the bare CBO and CuO samples, demonstrating that the composite exhibited a more efficient transfer and separation of photoinduced carriers [27]. Additionally, the EIS Nyquist plots are illustrated in Figure 6b. The semicircles in the high-frequency region correspond to the electron-transfer-limited process, which fit with the interfacial charge transfer resistance (R_{ct}) [33]. The arc radius of 30CBO/CuO (R_{ct} 2875 Ω) was observed to be the smallest when compared with those of bare CBO (R_{ct} 8293 Ω) and CuO (R_{ct} 5610 Ω), indicating the most efficient charge transfer for the composite [11]. The above results proved the positive effect of the heterojunction on the carrier separation.

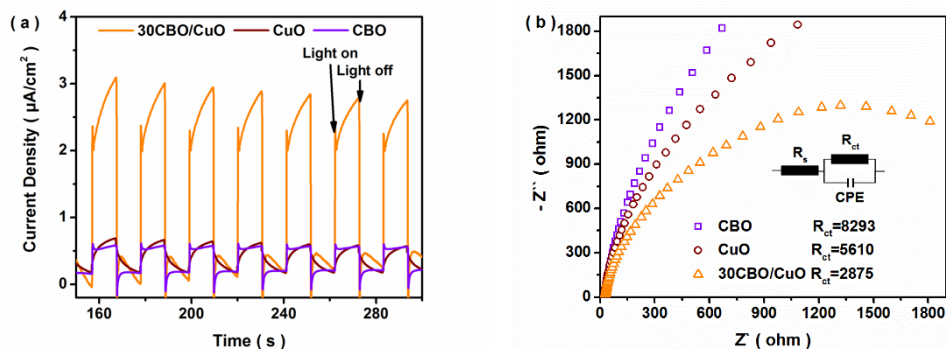


Figure 6. (a) I-t curves and (b) EIS Nyquist plots of CBO, CuO and 30CBO/CuO samples.

3.3. Possible Photocatalytic Mechanism

Based on the above experimental results and the band energy alignment of the CBO/CuO heterojunction, the enhanced photocatalytic activity for CO_2 reduction was deduced as follows. In the CBO/CuO composite, close contact between CBO and CuO caused the formation of a heterojunction, and an inner electrical field was established at the interface. Under visible-light illumination, the VB electrons of both components were excited. If the photoexcited charge carriers transferred following the common double-charge transfer mode (Figure 7a), the accumulated holes in the VB of the CBO component would not be able to oxidize H_2O to O_2 in thermodynamics, which was due to the VB potential of CBO (1.02 V vs. NHE) being more negative than the standard redox potential $E^\ominus(\text{O}_2/\text{H}_2\text{O})$ (1.23 V vs. NHE) [33]. Meanwhile, no products were found when using the CBO sample in the photocatalytic experiment. If the S-scheme charge transfer mechanism mode in

Figure 7b was employed, the catalytic sites of H₂O oxidization were constructed on the surface of the CuO component. In thermodynamics, the holes on VB of CuO could realize O₂ evolution from H₂O molecules, and the experimental results also proved that the catalytic process of CO₂ reduction and H₂O oxidization were realized for the bare CuO sample [34]. In situ-XPS measurements of 30CBO/CuO were conducted for a further demonstration of electron transfer across the heterojunction interface. As shown in Figure 7c,d, two peaks of Bi 4f obviously shifted towards the lower binding energy direction under illumination, and two characteristic peaks of Cu 2p reversely shifted, implying that the photoinduced electrons transferred from CuBi₂O₄ to CuO [35,36]. Combined with the above analysis, the CBO/CuO composite was a direct S-scheme heterojunction photocatalyst.

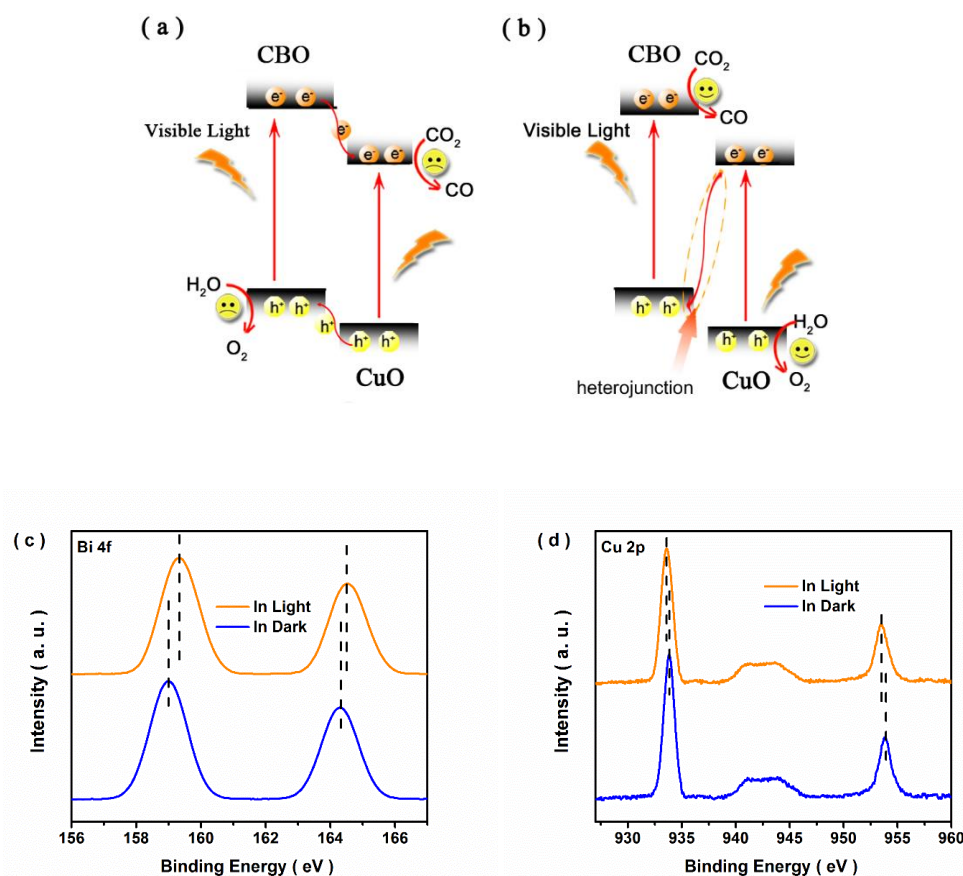


Figure 7. Schematic diagrams of the (a) common double-charge transfer and (b) S-scheme charge transfer modes in the CBO/CuO heterojunction; In situ-XPS spectra of (c) Bi 4f and (d) Cu 2p for the 30CBO/CuO sample.

Additionally, the conversion of CO₂ to CH₄ required eight electrons and four protons, while the conversion of CO₂ to CO only required two electrons. CO formation was more favorable with a lower surface density of photogenerated electrons, and CH₄ formation easily occurred with a higher surface density of photogenerated electrons [37,38]. Moreover, in the hydrogenation of CO₂ and CO, H adatoms were obtained from H₂O dissociation [37]. To explore the sample's hydrogen production ability, the photocatalytic activity for water splitting was studied for the CBO/CuO composite. Unfortunately, no product was discovered when using the 30CBO/CuO sample. After Pt loading, the H₂ yields for the Pt/CBO/CuO sample reached 12.4 μmol/g_{cat} after 8 h of illumination. Hence, the lack of aggregated electron sites and dissociation of H₂O to H adatoms on the CuBi₂O₄ surface might cause the selectivity of CO formation for CO₂ reduction in this study.

4. Conclusions

A series of CuBi₂O₄/CuO photocatalysts on glass substrates were synthesized by the ultra-fast spraying-calcination method. The optimal CBO/CuO composite exhibited a markedly higher photocatalytic performance of CO₂ reduction with H₂O vapor than those of bare CuBi₂O₄ and CuO, and the selectivity of the CO product was observably enhanced from below 18.5% to above 98.5%. After 9 h of visible-light illumination, the CO, CH₄ and O₂ yields reached 1599.1, 5.1 and 682.2 μmol/m², respectively. In the sixth cycling experiment, the yields of the main products decreased by less than 15%, and a high CO selectivity was still kept. The enhanced activity of CO₂ reduction was attributed to the efficient separation of photogenerated charge carriers that originated from the well-aligned staggered band structure of the CuBi₂O₄/CuO heterojunction. Based on the photocatalytic activity and in situ-XPS results, the S-scheme charge transfer mechanism was finally proposed. In summary, this study is expected to be useful in developing S-scheme photocatalysts for CO₂ reduction and to provide some meaningful information for a deep understanding of how photoinduced electrons transfer across contact interfaces.

Supplementary Materials: The following supporting information can be downloaded at: <https://www.mdpi.com/article/10.3390/nano12183247/s1>, Table S1: Binding energy and band gap of the obtained samples by XPS and DRS measurements; Figure S1: Survey spectra (a) and high resolution O 1s XPS spectra (b) of the CBO, CuO and 30CBO/CuO samples; Figure S2: TEM image of CBO (a) and CuO (b) samples (inset: diameter size distribution); Figure S3: Photocatalytic activity for different samples after 3 h of visible-light illumination.

Author Contributions: Conceptualization, W.S. and J.W.; software, X.Q., M.Z. and H.G.; validation, J.W. and J.M.; formal analysis, W.S., S.L. and J.W.; investigation, X.Q., W.Z. and J.W.; resources, J.W. and W.Z.; data curation, J.W.; writing—original draft preparation, W.Z. and J.W.; writing—review and editing, W.S.; supervision, W.S. and J.W.; project administration, W.S. and J.W.; funding acquisition, J.W., W.Z. and W.S. All authors have read and agreed to the published version of the manuscript.

Funding: This research was funded by the financial supports of the National Natural Science Foundation of China (No. 51802082), Key Scientific and Technological Project of Henan Province (No. 222102320100), Program for Science & Technology Innovation Talents in Universities of Henan Province (No. 21HATIT016), Key Project of Science and Technology Program of Xinxiang City (No. GC2021005) and National College Student Innovation and Entrepreneurship Training (No. 202110467024).

Data Availability Statement: Data are contained within the article.

Conflicts of Interest: The authors declare no conflict of interest.

References

1. Wang, K.; Ma, Y.; Liu, Y.; Qiu, W.; Wang, Q.; Yang, X.; Liu, M.; Qiu, X.; Li, W.; Li, J. Insights into the development of Cu-based photocathodes for carbon dioxide (CO₂) conversion. *Green Chem.* **2021**, *23*, 3207–3240. [[CrossRef](#)]
2. Shi, W.; Wang, J.-C.; Guo, X.; Tian, H.-L.; Zhang, W.; Gao, H.; Han, H.; Li, R.; Hou, Y. Ultra-fast construction of CuBi₂O₄ films supported Bi₂O₃ with dominant (0 2 0) facets for efficient CO₂ photoreduction in water vapor. *J. Alloys Compd.* **2021**, *890*, 161919. [[CrossRef](#)]
3. Wang, Y.; Wang, H.; He, T. Study on nanoporous CuBi₂O₄ photocathode coated with TiO₂ overlayer for photoelectrochemical CO₂ reduction. *Chemosphere* **2021**, *264*, 128508. [[CrossRef](#)]
4. Xu, Q.; Zhang, L.; Cheng, B.; Fan, J.; Yu, J. S-scheme heterojunction photocatalyst. *Chem* **2020**, *6*, 1543–1559. [[CrossRef](#)]
5. Bao, Y.; Song, S.; Yao, G.; Jiang, S. S-scheme photocatalytic systems. *Sol. RRL* **2021**, *5*, 2100118. [[CrossRef](#)]
6. Zhang, L.; Zhang, J.; Yu, H.; Yu, J. Emerging S-scheme photocatalyst. *Adv. Mater.* **2022**, *34*, 2107668. [[CrossRef](#)]
7. Xie, B.; Lovell, E.; Tan, T.H.; Jantarang, S.; Yu, M.; Scott, J.; Amal, R. Emerging material engineering strategies for amplifying photothermal heterogeneous CO₂ catalysis. *J. Energy Chem.* **2021**, *59*, 108–125. [[CrossRef](#)]
8. Wu, S.; Yu, X.; Zhang, J.; Zhang, Y.; Zhu, Y.; Zhu, M. Construction of BiOCl/CuBi₂O₄ S-scheme heterojunction with oxygen vacancy for enhanced photocatalytic diclofenac degradation and nitric oxide removal. *Chem. Eng. J.* **2021**, *411*, 128555. [[CrossRef](#)]
9. Dou, X.; Chen, Y.; Shi, H. CuBi₂O₄/BiOBr composites promoted PMS activation for the degradation of tetracycline: S-scheme mechanism boosted Cu²⁺/Cu⁺ cycle. *Chem. Eng. J.* **2022**, *431*, 134054. [[CrossRef](#)]

10. Luo, J.; Zhou, X.; Yang, F.; Ning, X.; Zhan, L.; Wu, Z.; Zhou, X. Generating a captivating S-scheme $\text{CuBi}_2\text{O}_4/\text{CoV}_2\text{O}_6$ heterojunction with boosted charge spatial separation for efficiently removing tetracycline antibiotic from wastewater. *J. Clean. Prod.* **2022**, *357*, 131992. [[CrossRef](#)]
11. Liu, J.; Huang, L.; Li, Y.; Yao, J.; Shu, S.; Huang, L.; Song, Y.; Tian, Q. Constructing an S-scheme $\text{CuBi}_2\text{O}_4/\text{Bi}_4\text{O}_5\text{I}_2$ heterojunction for light emitting diode-driven pollutant degradation and bacterial inactivation. *J. Colloid Interface Sci.* **2022**, *621*, 295–310. [[CrossRef](#)]
12. Shi, W.; Wang, J.-C.; Guo, X.; Qiao, X.; Liu, F.; Li, R.; Zhang, W.; Hou, Y.; Han, H. Controllable synthesized step-scheme heterojunction of CuBi_2O_4 decorated WO_3 plates for visible-light-driven CO_2 reduction. *Nano Res.* **2022**, *15*, 5962–5969. [[CrossRef](#)]
13. Pulipaka, S.; Boni, N.; Ummethula, G.; Meduri, P. $\text{CuO}/\text{CuBi}_2\text{O}_4$ heterojunction photocathode: High stability and current densities for solar water splitting. *J. Catal.* **2020**, *387*, 17–27. [[CrossRef](#)]
14. Edelmannová, M.; Lin, K.-Y.; Wu, J.C.S.; Troppová, I.; Čapek, L.; Kočí, K. Photocatalytic hydrogenation and reduction of CO_2 over CuO/TiO_2 photocatalysts. *Appl. Surf. Sci.* **2018**, *454*, 313–318. [[CrossRef](#)]
15. Taraka, T.P.Y.; Gautam, A.; Jain, S.L.; Bojja, S.; Pal, U. Controlled addition of Cu/Zn in hierarchical CuO/ZnO p-n heterojunction photocatalyst for high photoreduction of CO_2 to MeOH . *J. CO_2 Util.* **2019**, *31*, 207–214. [[CrossRef](#)]
16. Zhang, M.; Zhao, K.; Xiong, J.; Wei, Y.; Han, C.; Li, W.; Cheng, G. 1D/2D WO_3 nanostructure coupled with nanoparticulate CuO cocatalyst for enhancing solar-driven CO_2 photoreduction: The impact of the crystal facet. *Sustain. Energy Fuels* **2020**, *4*, 2593–2603. [[CrossRef](#)]
17. Xie, Z.; Xu, Y.; Li, D.; Chen, L.; Meng, S.; Jiang, D.; Chen, M. Construction of CuO quantum dots/ WO_3 nanosheets 0D/2D Z-scheme heterojunction with enhanced photocatalytic CO_2 reduction activity under visible-light. *J. Alloys Compd.* **2021**, *858*, 157668. [[CrossRef](#)]
18. Song, Y.; Ye, C.; Yu, X.; Tang, J.; Zhao, Y.; Cai, W. Electron-induced enhanced interfacial interaction of the CuO/BiOCl heterostructure for boosted CO_2 photoreduction performance under simulated sunlight. *Appl. Surf. Sci.* **2022**, *583*, 152463. [[CrossRef](#)]
19. Li, M.; Wu, Y.; Gu, E.; Song, W.; Zeng, D. Anchoring CuO nanospindles on g- C_3N_4 nanosheets for photocatalytic pollutant degradation and CO_2 reduction. *J. Alloys Compd.* **2022**, *914*, 165339. [[CrossRef](#)]
20. Nogueira, A.E.; Silva, G.T.S.T.; Oliveira, J.A.; Lopes, O.F.; Torres, J.A.; Carmo, M.; Ribeiro, C. CuO decoration controls Nb_2O_5 photocatalyst selectivity in CO_2 reduction. *ACS Appl. Energy Mater.* **2020**, *3*, 7629–7636. [[CrossRef](#)]
21. Park, H.S.; Lee, C.-Y.; Reiser, E. Photoelectrochemical reduction of aqueous protons with a $\text{CuO}/\text{CuBi}_2\text{O}_4$ heterojunction under visible light irradiation. *Phys. Chem. Chem. Phys.* **2014**, *16*, 22462. [[CrossRef](#)]
22. Hossain, M.K.; Samu, G.F.; Gandha, K.; Santhanagopalan, S.; Liu, J.P.; Janaky, C.; Rajeshwar, K. Solution combustion synthesis, characterization, and photocatalytic activity of CuBi_2O_4 and its nanocomposites with CuO and $\alpha\text{-Bi}_2\text{O}_3$. *J. Phys. Chem. C* **2017**, *121*, 8252–8261. [[CrossRef](#)]
23. Xu, Y.; Jian, J.; Li, F.; Liu, W.; Jia, L.; Wang, H. Porous CuBi_2O_4 photocathodes with rationally engineered morphology and composition towards high-efficiency photoelectrochemical performance. *J. Mater. Chem. A* **2019**, *7*, 21997–22004. [[CrossRef](#)]
24. Nogueira, A.C.; Gomes, L.E.; Ferencz, J.A.P.; Rodrigues, J.E.F.S.; Goncalves, R.V.; Wender, H. Improved visible light photoactivity of $\text{CuBi}_2\text{O}_4/\text{CuO}$ heterojunctions for photodegradation of methylene blue and metronidazole. *J. Phys. Chem. C* **2019**, *123*, 25680–25690. [[CrossRef](#)]
25. Wu, C.-H.; Onno, E.; Lin, C.-Y. CuO nanoparticles decorated nano-dendrite-structured CuBi_2O_4 for highly sensitive and selective electrochemical detection of glucose. *Electrochim. Acta* **2017**, *229*, 129–140. [[CrossRef](#)]
26. Wang, Y.; Cai, F.; Guo, P.; Lei, Y.; Xi, Q.; Wang, F. Short-time hydrothermal synthesis of CuBi_2O_4 nanocolumn arrays for efficient visible-light photocatalysis. *Nanomaterials* **2019**, *9*, 1257. [[CrossRef](#)] [[PubMed](#)]
27. Yuan, X.; Shen, D.; Zhang, Q.; Zou, H.; Liu, Z.; Peng, F. Z-scheme $\text{Bi}_2\text{WO}_6/\text{CuBi}_2\text{O}_4$ heterojunction mediated by interfacial electric field for efficient visible-light photocatalytic degradation of tetracycline. *Chem. Eng. J.* **2019**, *369*, 292–301. [[CrossRef](#)]
28. Cao, K.; Zhang, H.; Gao, Z.; Liu, Y.; Jia, Y.; Liu, H. Boosting glucose oxidation by constructing $\text{Cu}-\text{Cu}_2\text{O}$ heterostructures. *New J. Chem.* **2020**, *44*, 18449–18456. [[CrossRef](#)]
29. Shi, H.; Fan, J.; Zhao, Y.; Hu, X.; Zhang, X.; Tang, Z. Visible light driven $\text{CuBi}_2\text{O}_4/\text{Bi}_2\text{MoO}_6$ p-n heterojunction with enhanced photocatalytic inactivation of *E. coli* and mechanism insight. *J. Hazard. Mater.* **2020**, *381*, 121006. [[CrossRef](#)]
30. Wang, L.; Huang, T.; Yang, G.; Lu, C.; Dong, F.; Li, Y.; Guan, W. The precursor-guided hydrothermal synthesis of $\text{CuBi}_2\text{O}_4/\text{WO}_3$ heterostructure with enhanced photoactivity under simulated solar light irradiation and mechanism insight. *J. Hazard. Mater.* **2020**, *381*, 120956. [[CrossRef](#)]
31. Guo, F.; Shi, W.; Wang, H.; Han, M.; Guan, W.; Huang, H.; Liu, Y.; Kang, Z. Study on highly enhanced photocatalytic tetracycline degradation of type II $\text{AgI}/\text{CuBi}_2\text{O}_4$ and Z-scheme $\text{AgBr}/\text{CuBi}_2\text{O}_4$ heterojunction photocatalysts. *J. Hazard. Mater.* **2018**, *349*, 111–118. [[CrossRef](#)] [[PubMed](#)]
32. Kramm, B.; Laufer, A.; Reppin, D.; Kronenberger, A.; Hering, P.; Polity, A.; Meyer, B.K. The band alignment of $\text{Cu}_2\text{O}/\text{ZnO}$ and $\text{Cu}_2\text{O}/\text{GaN}$ heterostructures. *Appl. Phys. Lett.* **2012**, *100*, 094102. [[CrossRef](#)]
33. Jiang, Z.; Cheng, B.; Zhang, Y.; Wageh, S.; Al-Ghamdi, A.A.; Yu, J.; Wang, L. S-scheme ZnO/WO_3 heterojunction photocatalyst for efficient H_2O_2 production. *J. Mater. Sci. Technol.* **2022**, *124*, 193–201. [[CrossRef](#)]
34. Bhattacharyya, S.; Polavarapu, L.; Feldmann, J.; Stolarczyk, J.K. Challenges and prospects in solar water splitting and CO_2 reduction with inorganic and hybrid nanostructures. *ACS Catal.* **2018**, *8*, 3602–3635.

35. Wang, L.; Cheng, B.; Zhang, L.; Yu, J. In situ irradiated XPS investigation on S-scheme $\text{TiO}_2@Zn\text{In}_2\text{S}_4$ photocatalyst for efficient photocatalytic CO_2 reduction. *Small* **2021**, *17*, 2103447. [[CrossRef](#)] [[PubMed](#)]
36. Ge, H.; Xu, F.; Cheng, B.; Yu, J.; Ho, W. S-scheme heterojunction TiO_2/CdS nanocomposite nanofiber as H_2 -production photocatalyst. *ChemCatChem* **2019**, *11*, 6301–6309. [[CrossRef](#)]
37. Fu, J.; Jiang, K.; Qiu, X.; Yu, J.; Liu, M. Product selectivity of photocatalytic CO_2 reduction reactions. *Mater. Today* **2020**, *32*, 222–243. [[CrossRef](#)]
38. Zhan, P.; Yang, S.; Chu, M.; Zhu, Q.; Zhuang, Y.; Ren, C.; Chen, Z.; Lu, L.; Qin, P. Amorphous copper-modified gold interface promotes selective CO_2 electroreduction to CO. *ChemCatChem* **2022**, *14*, e202200109. [[CrossRef](#)]